

PAPER

## Thermally actuated micro-/nanoscale deformations for optical reconfigurations

To cite this article: Yinghao Zhao *et al* 2022 *J. Opt.* **24** 054007

View the [article online](#) for updates and enhancements.

### You may also like

- [A Kirigami shape memory polymer honeycomb concept for deployment](#)  
Robin M Neville, Jianguo Chen, Xiaogang Guo *et al.*
- [Kirigami-inspired dual-parameter tactile sensor with ultrahigh sensitivity, multimodal and strain-insensitive features](#)  
Jarkko Tolvanen, Jari Hannu and Heli Jantunen
- [Inkjet printed kirigami inspired split ring resonator for disposable, low cost strain sensor applications](#)  
Ahmed Salim, Aqeel Hussain Naqvi, Eiyong Park *et al.*



**IOP | ebooks™**

Bringing together innovative digital publishing with leading authors from the global scientific community.

Start exploring the collection—download the first chapter of every title for free.

# Thermally actuated micro-/nanoscale deformations for optical reconfigurations

Yinghao Zhao<sup>1</sup> , Chang-Yin Ji<sup>1,\*</sup>, Hengzhang Yang<sup>2</sup>, Yang Wang<sup>1</sup>, Huikai Xie<sup>2</sup>   
and Jiafang Li<sup>1,3,\*</sup>

<sup>1</sup> Key Lab of Advanced Optoelectronic Quantum Architecture and Measurement (Ministry of Education), Beijing Key Lab of Nanophotonics & Ultrafine Optoelectronic Systems, and School of Physics, Beijing Institute of Technology, Beijing 100081, People's Republic of China

<sup>2</sup> School of Integrated Circuits and Electronics, Beijing Institute of Technology, Beijing 100081, People's Republic of China

<sup>3</sup> Yangtze Delta Region Academy of Beijing Institute of Technology, Jiaxing 314019, People's Republic of China

E-mail: [jcyinbit@bit.edu.cn](mailto:jcyinbit@bit.edu.cn) and [jiafangli@bit.edu.cn](mailto:jiafangli@bit.edu.cn)

Received 10 January 2022, revised 19 February 2022

Accepted for publication 24 February 2022

Published 8 April 2022



## Abstract

The unique three-dimensional (3D) deformations caused by nano-kirigami have enabled a new degree of freedom for reconfigurable optics. Here, we demonstrate a facile nano-kirigami method that can create 3D deformed structures, which can flexibly manipulate optical properties using thermally actuated micro-/nanoscale deformations. By connecting four pairs of thermal actuators to the four sides of a gradient metasurface, large-angle beam steering ( $\sim 90^\circ$ ) can be achieved by adjusting the temperature of the actuators. The amplitude of circular dichroism can be adjusted by thermally actuating micro-/nanoscale deformations. The 2D-to-3D transformation of the curved arm structure on metallic substrate results in enhanced structural absorption, inducing an almost perfect absorption at specific wavelengths. Curved asymmetric structures can also be created by thermally actuated micro-/nanoscale deformations, which provides a novel method for cross-polarized light conversion. The proposed design with thermally actuated micro-/nanoscale deformations provides a new methodology to explore versatile reconfigurable functionalities.

**Keywords:** nano-kirigami, optical reconfiguration, thermal actuation, thermal stresses, micro-/nanoscale deformations

(Some figures may appear in colour only in the online journal)

## 1. Introduction

Nano-kirigami [1–4], a novel scheme to achieve the complex shape transformation from two-dimensional (2D) precursors to three-dimensional (3D) architectures, has been used to construct a variety of 3D micro-/nanostructures with flexible

functionalities and reconfiguration capability. This method makes use of mechanical actuation or stress induction to create unique transformations such as folding and twisting, which could break up linear additive thinking [5–7] in the traditional on-chip 3D micro-/nanofabrications [8–10]. One of the benefits of the unconventional 3D geometries created by kirigami at the nanoscale is the additional spatial freedom and rich physical characteristics [11, 12], and the other, even more important benefits, are the fascinating optical properties

\* Authors to whom any correspondence should be addressed.

such as giant optical chirality [13], elastic wide-angle gratings [14], Fano-resonant metamaterials [15], etc. Moreover, besides the superior optical properties, the reconfiguration capability based on the reversible spatial displacement realized by mechanical [11] and electromechanical [1] actuation have been demonstrated. Nevertheless, exploring new reconfigurable strategies is still essential.

Meanwhile, the reconfiguration capability based on the reversible displacement has been widely employed in optical microelectromechanical systems (MEMS) [16], like the movable micromirrors of digital micromirror devices [17] commercialized successfully in digital light processing. Among different driving mechanisms in optical MEMS, the electro-thermal actuation [18–21] have continuously drawn attention due to the large vertical displacements of hundreds of microns at low driving voltages, offering a reliable idea for the reconfigurable strategy of the nano-kirigami.

In this article, we propose a thermal reconfiguration method to transform the 2D nanopatterns into 3D deformed nanostructures. When temperature varies, thermal stresses are introduced due to mismatches of the thermal expansion coefficient between adjacent thin films, leading to the spontaneous curving or folding. With the associated vertical deformations, the large angle optical beam deflection can be achieved in the metasurfaces combined with the MEMS. For the single structure, intrinsic chiroptical responses can be achieved in the 3D structure, of which the strength can be tuned via the externally applied temperature. Meanwhile, the 2D-to-3D transformation also induces an almost perfect absorption at specific wavelengths. Additionally, tilted asymmetrical structures created by thermal nano-kirigami are proposed to convert left-handed circularly polarized (LCP) light into right-handed circularly polarized (RCP) light. The proposed thermal reconfiguration method and nanostructures could offer new opportunities for reconfigurable systems, nanophotonics [22], MEMS, etc.

## 2. Results and discussions

### 2.1. Large angle beam steering for metasurface

The designed structure is schematically depicted in figure 1(a). The central device is connected by four pairs of actuators, which can realize the function of abnormal reflection. The actuator consists of two sets of opposite Al/SiO<sub>2</sub>, SiO<sub>2</sub>/Al/SiO<sub>2</sub> and SiO<sub>2</sub>/Al layers. The delicate connection of these tiny structures with metal and dielectric materials could be achieved with the help of state-of-the-art nanomanufacturing [20]. The unit cell of the device in figure 1(a) is shown in figure 1(b). The structure is composed of nanoantennas of different lengths. The nanoantennas have the same thickness (30 nm) and width ( $W = 90$  nm). The thicknesses of MgF<sub>2</sub> and gold films are set as 50 nm and 130 nm, respectively. By carefully choosing the length of the Au nanoantennas, their scattering phase can cover the range of  $2\pi$ . Here, the design of the ten Au nanoantennas in figure 1(b) is based on the gradient metasurface in [23], in which the length of the nanoantennas are

set as 40, 40, 106, 106, 128, 128, 150, 150, 260, and 260 nm. The distance between two adjacent nanoantennas along the  $x$  direction is 120 nm. The period of the supercell in figure 1(b) along the  $x$  and  $y$  directions is  $P_x = 1.2 \mu\text{m}$  and  $P_y = 0.3 \mu\text{m}$ , respectively. Numerical simulations are all conducted by using the COMSOL software based on the finite element method. For example, the thermally actuated structural deformations are modelled by the solid mechanics module. The material properties are described with linear elastic material and their attributes are modelled by thermal expansion. The thermal expansion coefficients of Al, SiO<sub>2</sub> and Ag are  $23.1\text{e}^{-6}$  1/K,  $0.5\text{e}^{-6}$  1/K and  $18.9\text{e}^{-6}$  1/K, respectively [24]. The refractive indices of Au and Ag are described by the Lorentz–Drude model [25]. The refractive indices of the MgF<sub>2</sub> and SiO<sub>2</sub> are set to 1.37 and 1.45, respectively. All material parameters can be found from the material database of the COMSOL software. The physical mechanism behind the deformations is that the temperature difference induces strain and the strain is equal to  $\alpha\Delta T$ , where  $\alpha$  and  $\Delta T$  are the thermal expansivity and temperature difference, respectively. The final structural deformations are obtained under the mechanical equilibrium. Due to the mismatch of thermal expansion coefficients between materials Al and SiO<sub>2</sub>, the central device can be tilted with respect to the XY plane by controlling the temperature applied to actuators, as shown in figure 1(c). It should be pointed out that the deposition temperature, designed based on the realistic device in [24], is 600 K for all thin-film layers, which means the as-deposited structure (at 600 K) is in 2D without deformation at 600 K, as shown in the left of figure 1(c). As shown on the right in figure 1(c), a tilt angle of about  $29^\circ$  can be obtained when all the actuators in one opposing pair are set at 450 K, while the actuators of the other pair are set at 300 K and 600 K, respectively. Such variations in temperature of the beams could be implemented by applying different voltages to the Pt layer resistors embedded along the beams, which are insulated from the Al layer and the substrate by thin layers of SiO<sub>2</sub> [24]. Importantly, the morphology of the central device is not deformed when it is tilted.

We demonstrate that the temperature induced global deformation can provide an important scheme to realize the function of dynamically reconfigurable anomalous reflection angle of the metasurface. According to the generalized Snell's law [26, 27], one can get the reflection angle  $\theta_r = \sin^{-1}\left(\frac{\lambda}{P_x} + \sin(\theta_i)\right)$ .  $\lambda$  and  $\theta_i$  are the wavelength and incident angle of the incident light, respectively. Here, we choose to illuminate the central device from the top with y-polarized light with wavelength of  $\lambda = 850$  nm and  $\theta_i = 0^\circ$ . For convenience we denote  $\theta_t$  as the tilt angle of the central device. When the central device is tilted, the  $\theta_r$  needs to be corrected as  $\theta_r + 2\theta_t$ . The figure 1(d) shows the results of y-polarized field distributions reflected by the metasurface with different tilt angle  $\theta_t$ . It can be seen that the  $\theta_r$  is equal to  $45^\circ$  for  $\theta_t = 0^\circ$ , which agrees well with the generalized Snell's law. Interestingly, the angle of reflection is significantly modulated when the structure is tilted. The reflection angles are  $71^\circ$  and  $85^\circ$  for  $\theta_t$  with  $10^\circ$  and  $15^\circ$ , respectively. The small deviation of the reflection angle with respect to  $\theta_r + 2\theta_t$  is caused by the

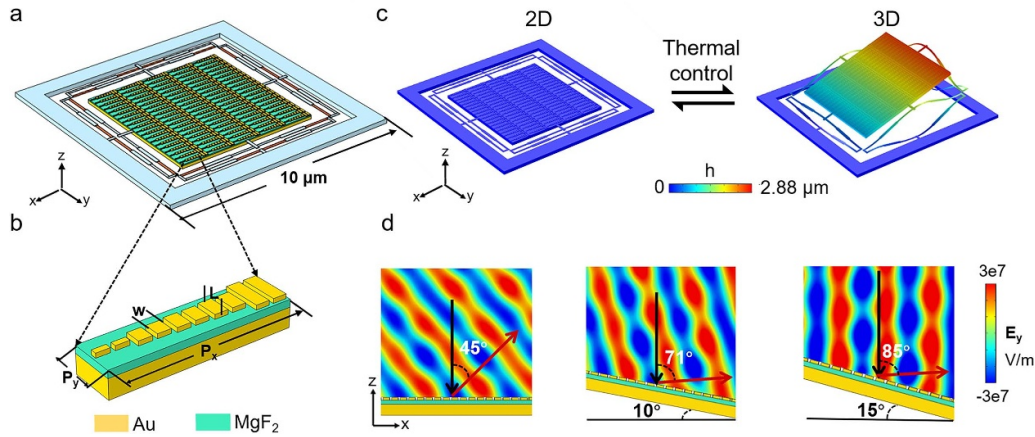


**Figure 1.** Global deformation for beam steering. (a) Illustration of the designed structure, including a gradient metasurface in the center and four pairs of actuators connected between the central part and SiO<sub>2</sub> supporting frame. (b) Schematic of the unit cell consisting of a 30 nm thick Au nanoantenna and a 130 nm thick Au film separated by a 50 nm thick MgF<sub>2</sub> spacer. The top Au nanoantennas consists of ten units with length of 40, 40, 106, 106, 128, 128, 150, 150, 260, and 260 nm, respectively. Other parameters are fixed as  $W = 90$  nm,  $P_x = 1.2$   $\mu$ m,  $P_y = 0.3$   $\mu$ m. (c) Schematic diagram of the thermal reconfiguration. (d)  $E_y$  field distributions in the  $xz$  plane reflected by the metasurface with tilting angle of 0°, 10°, and 15°, respectively, under the normal incidence of  $y$ -polarized light.

angular dispersion of the reflected phase of the nanoantennas. The efficiencies of the metasurface with the tilting angle of 0°, 10°, and 15° are 0.75, 0.66 and 0.56, respectively. Thus, the large angle beam steering and reconfiguration can be achieved by controlling the temperature of the actuators.

## 2.2. Chirality switching of 2D and 3D curved arm structure

The temperature induced local deformation can also be used to modulate the chiroptical responses. In order to realize the pixelated reconfiguration of metasurface itself, we have redesigned the curved arm structure which is arranged in a hexagonal lattice with lattice period of 2.5  $\mu$ m, as shown in figure 2(a). The central Ag disk is connected by three curved arms and the whole structural unit has threefold rotation ( $C_3$ ) symmetry. The design of the supported central disk is aimed for multi-functional applications of the structure, such as a beam deflector and a platform for hybrid devices (as the central part in figure 1). It should be pointed out that the chiral effects and the dynamic optical effects presented in this paper are due to plasmonic resonances in the deformed arms (see below analysis). Each curved arm consists of three layers, i.e. a bottom SiO<sub>2</sub> layer, an intermediate Ag layer and a top SiO<sub>2</sub> layer. Because the different thermal expansion coefficient of Ag and SiO<sub>2</sub>, the stress induced by temperature difference brings out the upward deformation of the arms when temperature is changed, as shown in figure 2(b). As the deposition temperature changes from 600 K to 300 K, figure 2(b) shows that the 2D structure will be deformed out-of-plane into a 3D structure. The thermal stress induced maximum out-of-plane height is about 180 nm. It can be expected that the chiroptical response can be significantly enhanced by the breaking of mirror symmetry caused by the out-of-plane deformation.

The transmission spectrum of the 2D structure under the normal incidence with circularly polarized light (CPL) is

plotted in figure 2(c). It can be seen that the spectra coincide perfectly for RCP and LCP light. Due to the  $C_3$  symmetry, the circular dichroism (CD) is defined as  $CD = A_{LCP} - A_{RCP} = T_{RCP} - T_{LCP}$ , where  $A_{LCP}$  ( $A_{RCP}$ ) and  $T_{LCP}$  ( $T_{RCP}$ ) are the absorption and total transmission of LCP (RCP) light, respectively. In such case, the 2D structure does not have any CD [28]. The 2D structure has three resonant modes in the spectral range under consideration (see figure 2(c)). Different to the 2D structure, the transmission spectrum is different at the resonant wavelength under the LCP and RCP light incidence for the 3D structure. Especially at the resonant wavelength of 3.4  $\mu$ m for the second resonant mode, the transmission difference between LCP and RCP light is significantly increased, which means the 3D deformed curved arm structure exhibits clear CD responses under  $T = 300$  K, as shown in figures 2(d) and (e). Meanwhile, the amplitudes of the CD peak can be changed by the different temperature, as shown in figure 2(e). When the temperature is 600 K, the 2D structure has zero CD responses in a wide spectral range. As the temperature decreases from 600 K to 300 K, the value of CD peak is enhanced from 0 to 0.4, as shown in figure 2(e). The fundamental physics for such enhanced difference in CPL absorption is that the arm structure is highly deformed at 300 K, which breaks the mirror symmetry of the structure more effectively. As a result, the deformed structure possesses more pronounced chiroptical responses [29, 30]. In addition to CD enhancement, the resonant wavelength of the CD peak is slightly blue shifted as the temperature changes from 600 K to 300 K. The simulation results clearly prove the feasibility of dynamic chirality switching by thermally actuated micro-/nanoscale deformations.

## 2.3. Polarization insensitive absorption enhancement

In addition to manipulate the spin states of light, optical perfect absorption [31, 32] is also crucial in a widespread application,



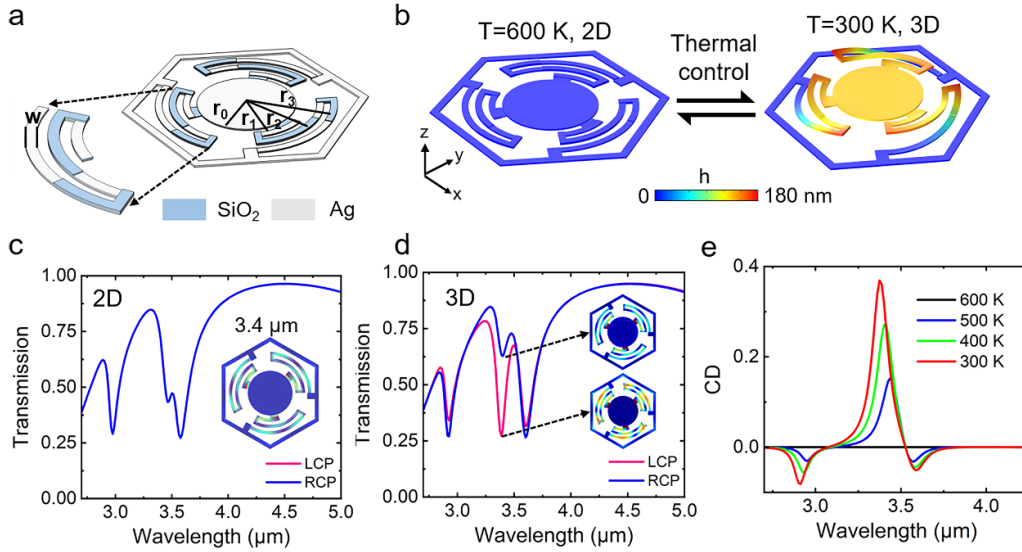


**Figure 2.** Local deformation for chirality switching. (a) Schematic of the curved arm structure with period of  $2.5 \mu\text{m}$ . The unit cell is arranged in a hexagonal lattice. The  $20 \text{ nm}$  thick Ag disk is connected by three arms with length of  $3.45 \mu\text{m}$  consisting of a bottom  $\text{SiO}_2$  layer, an intermediate Ag layer, and a top  $\text{SiO}_2$  layer. Other parameters are fixed as  $w = 80 \text{ nm}$ ,  $r_0 = 0.6 \mu\text{m}$ ,  $r_1 = 0.7 \mu\text{m}$ ,  $r_2 = 0.86 \mu\text{m}$  and  $r_3 = 1.02 \mu\text{m}$ . (b) Schematic diagram of the thermal reconfiguration. The 3D curved arm structure can be obtained under the deposition temperature changing from  $600 \text{ K}$  to  $300 \text{ K}$ , which results in the maximum upward deformation height of  $180 \text{ nm}$ . (c), (d) Simulated transmission spectra of the structure 2D and 3D under normal incidence of left-handed circularly polarized (LCP) and right-handed circularly polarized (RCP) wave. It can be seen that the electric field distributions are more pronounced on and near the curve arms at the optical resonances (inset: of 3D structure under LCP). Thus, it is believed that the optical resonances are more favorably supported by the irregularly deformed arms. (e) Calculated CD of initial 2D curved arm structure and 3D curved arm structure deformed by different temperature. The CD is defined as  $\text{CD} = A_{\text{LCP}} - A_{\text{RCP}} = T_{\text{RCP}} - T_{\text{LCP}}$  due to its threefold rotational symmetry.

such as solar energy [33, 34], optical sensing [35], all-optical multichannel logic [36] and so on. Here, the designed nanostructure is presented in figure 3(a), which consists of curved arm structure in figure 2(a), a  $\text{SiO}_2$  supporting layer and Ag substrate. The Ag substrate is thick enough to prevent the light transmission under the normally incident LCP light. Therefore, the absorption is defined as  $A = 1R$ , where  $R$  is reflection. The deformed structures from different perspectives are shown in figures 3(b) and (c). The structure is obtained by changing the temperature from  $600 \text{ K}$  to  $300 \text{ K}$ . The upward deformation maximum height is  $180 \text{ nm}$  and the thickness of  $\text{SiO}_2$  layer is  $d$ . The absorption spectra of the 2D and 3D structures with different  $d$  under LCP incidence are shown in figures 3(d)–(f). It can be seen that the absorption spectra are different between the 2D and 3D nanostructures. Absorption peak values at certain specific wavelengths are significantly enhanced with the structure deformed from 2D to 3D. For example, as  $d = 20 \text{ nm}$ , the absorption of the 2D nanostructure is close to zero at wavelengths of  $3.25 \mu\text{m}$  and  $3.96 \mu\text{m}$ , respectively, while the absorption of the deformed structure is significantly enhanced and close to  $0.8$ , as shown in figure 3(d). The thickness of  $\text{SiO}_2$  layer also significantly affects the absorption. It is worth noting that the perfect absorption is achieved under  $d = 100 \text{ nm}$  for the 3D structure. Compared with the 2D structures, the 3D structures can realize multiple strong absorption peaks. Meanwhile, the wavelengths of absorption peaks of the structure move towards the short wavelengths with the increase of the thickness of the supported intermediate layer, which

means specific absorption wavelengths can be selected by adjusting the thickness of the intermediate layer. For example, the wavelength of the first absorption peak corresponding to the 3D structure moves from  $3.25$  to  $3.2$  and  $3.1 \mu\text{m}$ , respectively, with  $d$  changed from  $20$  to  $50$  and  $100 \text{ nm}$ .

In order to quantitatively describe the changes in absorption caused by the deformation of curved arm structure, the corresponding contrast in absorption [37] of 2D and 3D structures are defined as  $\Delta A = A_{2\text{D}} - A_{3\text{D}}$ , as shown in figures 3(h)–(j). As  $d = 20 \text{ nm}$ , the  $\Delta A$  can reach nearly  $0.75$ . It is worth noting in figure 3(i) that  $\Delta A$  can reach nearly unit at the wavelength of  $3.75 \mu\text{m}$ . Consequently, the above discussion provides that 3D deformed nanostructure with subwavelength properties can possess unique enhanced optical absorption properties.

To further understand the enhanced absorption, the electric field distributions of 2D and 3D structures at the same wavelength are shown in figure 4. The results of  $d = 20 \text{ nm}$  is shown in figure 4(a). It can be seen that the electric field is significantly enhanced at the curve arms of the 3D structure for the absorption peak wavelengths. It is well known that surface plasmon polaritons (SPPs) cannot not be coupled to the smooth metallic surface effectively due to the mismatch in wavevectors. Here, the deformations significantly increase arm distortion and thereby certain SPP modes can be efficiently excited at certain wavelengths for the 3D structures that meet the coupling condition between SPPs and incident light. The efficiently coupled SPPs can greatly enhance the electric

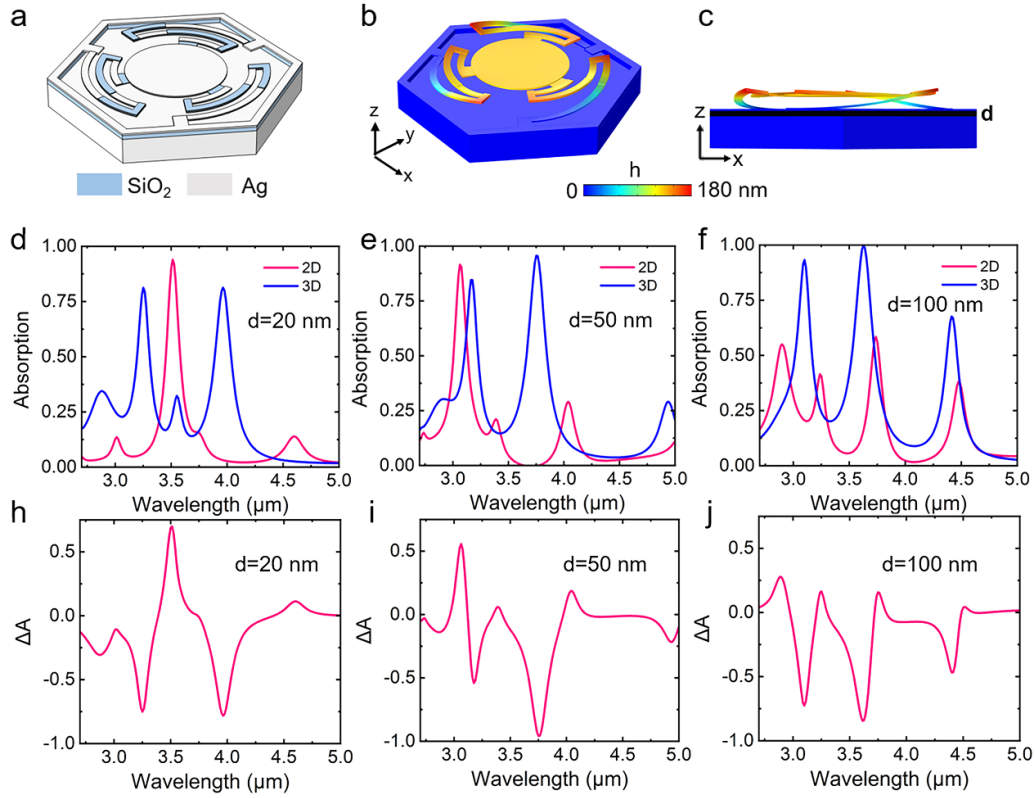


**Figure 3.** Local deformation for absorption engineering. (a) The curved arm structure is suspended on SiO<sub>2</sub> frame with thickness  $d$ , which is supported by the bottom Ag substrate. (b) Side view and (c) front view of the schematic of the 3D structure. The maximum upward deformation height is 180 nm. (d)–(f) Absorption spectra of 2D (pink) and 3D (blue) curved arm structure under the normally incident LCP light. The thickness of SiO<sub>2</sub> is  $d = 20, 50$ , and  $100$  nm, respectively. It can be seen that the perfect absorption is achieved under  $d = 100$  nm. (h)–(j) Calculated corresponding contrast in absorption ( $\Delta A = A_{2D} - A_{3D}$ ) of the 2D and 3D curved arm structures.

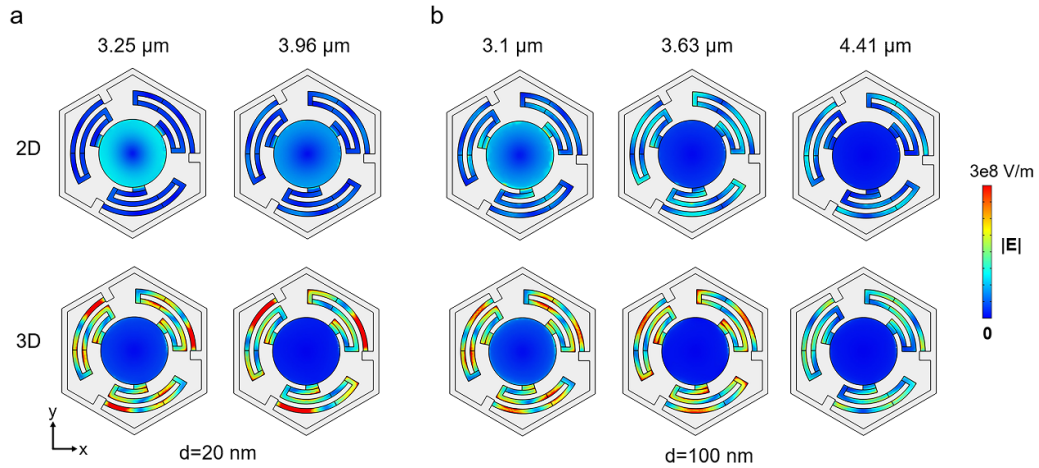


**Figure 4.** Enhanced field distributions by deformations. (a), (b) Simulated electric field distribution of the 2D (top) and 3D (bottom) structures in  $xy$  plane at the absorption peak of the 3D curved arm structure.

field. Meanwhile, the optical loss density is determined by  $\frac{1}{2}\omega\epsilon_{\text{im}}(\mathbf{r})|\mathbf{E}(\mathbf{r})|^2$ . Here  $\omega$ ,  $\epsilon_{\text{im}}(\mathbf{r})$  and  $|\mathbf{E}(\mathbf{r})|^2$  are the angular frequency of the light, imaginary part of the dielectric function and electric field distributions, respectively. Thus, the enhanced electric field in the legs increases corresponding absorption. The electric field distributions in figure 4(b) show the similar results in figure 4(a). The values of  $d$  mainly affect the coupling of the superstructure and the Ag substrate. Thus,

one can choose suitable  $d$  to reduce reflection and increase absorption.

#### 2.4. Cross-polarized light conversion of curved asymmetric structure

The chiroptical responses and perfect absorption induced by deformation are based on the temperature change of all the

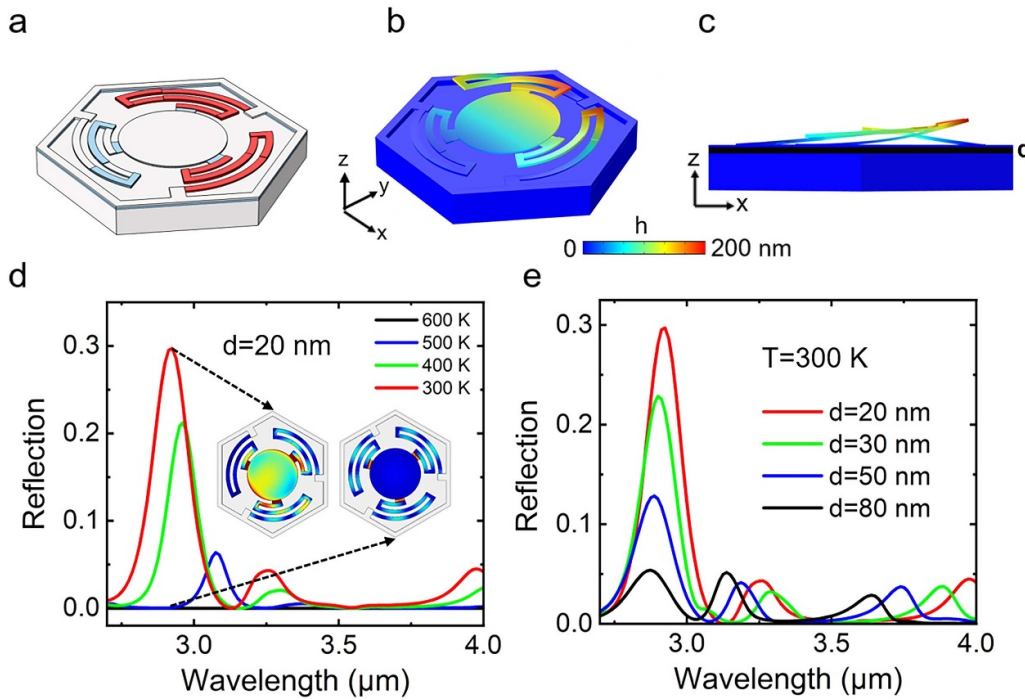


**Figure 5.** Asymmetric deformations for cross-polarized light conversion. (a) Schematic diagram of the thermal reconfiguration of curved asymmetric structure. Asymmetric deformation can be achieved by setting 300 K in the arms which are marked as red while the other one remains the same (600 K). (b) Side-view and (c) front view of the schematic of the curved arm asymmetric structure with a tilting angle of  $\sim 10^\circ$ . The thickness of the  $\text{SiO}_2$  supporter (in black) is  $d$ . (d) Cross-polarized reflection spectra of the 3D curved arm asymmetric structure with  $d = 20 \text{ nm}$  under different temperature. It can be seen that the electric field distributions are more pronounced on and near the central disk at the optical resonances for  $T = 300 \text{ K}$ . Compared with the electric field distributions of the  $T = 300 \text{ K}$  and  $T = 600 \text{ K}$ , it can be found that the enhanced cross-polarization conversion efficiency results from the change of optical mode of the central disk. (e) Calculated cross-polarized reflection spectra with same temperature 300 K for different thickness  $d$ .

three arms. The whole structure has  $C_3$  symmetry. Such rotation symmetry imposes some restrictions on the transmission and reflection properties. For example, the cross-polarized reflection and transmission cannot be achieved under the  $C_3$  symmetry. Structures lacking any point group symmetry can exhibit more complex optical responses, providing abundant freedom to manipulate the behaviors of light [38]. The asymmetric deformation can be achieved by setting different temperature in the three arms, resulting in the breaking of  $C_3$  symmetry. For example, as shown in figure 5(a), the two arms marked in red were lowered by 300 K on the basis of deposition temperature (600 K), while the other one was kept at deposition temperature without deformation. The deformed structure is shown in figures 5(b) and (c), with a tilt angle of about  $10^\circ$ . The tilted asymmetric deformation breaks the  $C_3$  symmetry of the structure. As a result, the reflection light has cross-polarized component [39], as shown in figure 5(d). The maximum conversion efficiency of the cross polarization is enhanced with the temperature gradually decreases under LCP incidence for  $d = 20 \text{ nm}$ . The maximum conversion efficiency of the cross polarization is up to 0.3 when the temperature is setting at 300 K at the wavelength  $2.9 \mu\text{m}$ . Meanwhile, with the decrease of temperature relative to deposition temperature, the peak wavelength of the reflected cross-polarization light reveals a blue shift, as shown in figure 5(d). We also investigate the effect of thickness  $d$  on cross-polarized light conversion, as

shown in figure 5(e). It can be seen that the maximum conversion efficiency is dependent on  $d$  near the wavelength  $2.9 \mu\text{m}$  since  $d$  affects the coupling properties of the deformed structure to the Ag substrate. As shown in figure 5(e), the maximum conversion efficiency near  $2.9 \mu\text{m}$  can be increased from 0.05 to 0.3 with  $d$  changed from 80 to 20 nm.

### 3. Conclusion

In conclusion, we have introduced a novel scheme of thermally actuated micro-/nanoscale deformations to achieve different reconfigurable optical functionalities. By introducing thermal stresses to produce global deformation, the large-angle optical beam deflection was dynamically tuned by employing the temperature. More importantly, the thermal stresses guided shape transformation has been employed to induce the local deformation of the unit cell. It was found that the breaking of mirror symmetry greatly enhanced the chiroptical responses. Meanwhile, the 2D-to-3D transformation of curved arm structure on metallic substrate significantly enhanced the absorption of the nanostructures, resulting in an almost perfect absorption for some special wavelengths. Additionally, the curved asymmetric structure was also created by the thermally actuated micro-/nanoscale deformations, which provides a novel method for cross-polarized light conversion. Therefore, the

proposed thermally actuated shape transformation in this work could provide a new scheme for reconfigurable photonic systems, as well as dynamic applications in quasi-flat optical platforms.

## Data availability statement

All data that support the findings of this study are included within the article (and any supplementary files).

## Acknowledgments

This work is supported by the National Natural Science Foundation of China under Grant No. 61975016, the Science and Technology Project of Guangdong (2020B010190001), Natural Science Foundation of Beijing Municipality (1212013 and Z190006), and Beijing Municipal Science & Technology Commission, Administrative Commission of Zhongguancun Science Park No. Z211100004821009, and the China Postdoctoral Science Foundation (2021M700436). The authors thank Analysis & Testing Center at Beijing Institute of Technology, and Zhiwei Song of National Center for Nanoscience and Technology for assistance.

## ORCID iDs

Yinghao Zhao  <https://orcid.org/0000-0001-9535-4896>  
Huikai Xie  <https://orcid.org/0000-0002-8393-0021>

## References

- [1] Chen S *et al* 2021 *Nat. Commun.* **12** 1299
- [2] Chen S, Wei W, Liu Z, Liu X, Feng S, Guo H and Li J 2020 *Photonics Res.* **8** 1177–82
- [3] Han Y U, Liu Z, Chen S, Liu J, Wang Y and Jiafang L 2020 *Photonics Res.* **8** 1506–11
- [4] Liu Z, Du H, Li J, Lu L, Li Z Y and Fang N X 2018 *Sci. Adv.* **4** 4436
- [5] Gansel J K, Thiel M, Rill M S, Decker M, Bade K, Saile V, Freymann G V, Linden S and Wegener M 2009 *Science* **325** 1513–5
- [6] Liu N, Guo H, Fu L, Kaiser S, Schweizer H and Giessen H 2008 *Nat. Mater.* **7** 31–37
- [7] Turner M, Saba M, Zhang Q, Cumming B P, Schröder-Turk G E and Gu M 2013 *Nat. Photon.* **7** 801–5
- [8] Lu W E *et al* 2013 *Opt. Mater. Express* **3** 1660–73
- [9] Noh J H, Fowlkes J D, Timilsina R, Stanford M G, Lewis B B and Rack P D 2015 *ACS Appl. Mater. Interfaces* **7** 4179–84
- [10] Saracogullari N, Gundogdu D, Ozdemir F N, Soyer Y and Erel-Goktepe I 2021 *Colloids Surf. A* **617** 126313
- [11] Liu Z, Cui A, Li J and Gu C 2018 *Adv. Mater.* **31** 1802211
- [12] Xu S *et al* 2015 *Science* **347** 154–9
- [13] Choi W J, Cheng G, Huang Z, Zhang S, Norris T B and Kotov N A 2019 *Nat. Mater.* **18** 1
- [14] Xu L, Wang X, Kim Y, Shyu T C, Lyu J and Kotov N A 2016 *ACS Nano* **10** 6156–62
- [15] Liu Z, Li J, Liu Z, Li W, Li J, Gu C and Li Z Y 2017 *Sci. Rep.* **7** 1–9
- [16] Piyawattanametha W, Ra H, Mandella M J, Liu J, Wong L K, Du C B, Wang T D, Contag C H, Kino G S and Solgaard O 2007 Highly adaptable MEMS-based display with wide projection angle
- [17] Hornbeck L J and Wu M H 1997 *SPIE* **3013** 27–40
- [18] Wu L and Xie H 2008 *Sens. Actuators A* **145–146** 371–9
- [19] Lin L, Pal S and Xie H 2011 *Solid-State Sensors, Actuators & Microsystems Conf.* pp 2522–5
- [20] Samuelson S R, Sean R and Xie H 2014 *J. Microelectromech. Syst.* **23** 39–49
- [21] Samuelson S R and Xie H 2012 *J. Microelectromech. Syst.* **23** 39–49
- [22] Chen Z and Segev M 2021 *eLight* **1** 1–12
- [23] Sun S *et al* 2012 *Nano Lett.* **12** 6223–9
- [24] Jia K, Pal S and Xie H 2009 *J. Microelectromech. Syst.* **18** 1004–15
- [25] Prucha E J and Palik E D 1998 *Handbook of Optical Constants of Solids* vol 3
- [26] Wang C, Liu W, Li Z, Cheng H, Li Z, Chen S and Tian J 2018 *Adv. Opt. Mater.* **6** 1701047
- [27] Yang Y, Wang W, Moitra P, Kravchenko I I, Briggs D P and Valentine J 2014 *Nano Lett.* **14** 1394–9
- [28] Alpegiani F, Bliokh K Y, Nori F and Kuipers L 2018 *Phys. Rev. Lett.* **120** 243605
- [29] Bliokh K Y and Nori F 2011 *Phys. Rev. A* **83** 4762–7
- [30] Schaferling M, Dregely D, Hentschel M and Giessen H 2012 *Phys. Rev. X* **2** 4186–90
- [31] Liu N, Mesch M, Weiss T, Hentschel M and Giessen H 2010 *Nano Lett.* **10** 2342–8
- [32] Tao H, Landy N I, Bingham C M, Zhang X, Averitt R D and Padilla W J 2008 *Opt. Express* **16** 7181–8
- [33] An Y, Zhao Y, Ma T and Li X 2019 *J. Semiconduct.* **40** 050403
- [34] Niklasson G A and Granqvist C G 1983 *J. Mater. Sci.* **18** 5347–534
- [35] Wang G, Wang Y, Chen L and Choo J 2010 *Biosens. Bioelectron.* **25** 1859–68
- [36] Papaioannou M, Plum E, Valente J, Rogers E and Zheludev N I 2016 *APL Photonics* **1** 354–157
- [37] Aieta F, Genevet P, Kats M A, Yu N, Blanchard R, Gaburro Z and Capasso F 2012 *Nano Lett.* **12** 4932
- [38] Zhihua Y X, Hu J, Zeng Y, Zeng W and J J P 2020 *J. Semicond.* **41** 38–44
- [39] Ishikawa A, Hara S, Tanaka T, Hayashi Y and Tsuruta K 2017 *Sci. Rep.* **7** 3205